

# Lensing Model of MACS J1149.5+2223 I: Cluster Mass Reconstruction

S. Rau<sup>1</sup> <sup>\*</sup>, S. Vegetti<sup>1</sup>, S. D. M. White<sup>1</sup>

<sup>1</sup>Max-Planck Institute for Astrophysics, Karl-Schwarzschild Str. 1, D-85748, Garching, Germany

13 June 2022

## ABSTRACT

Measurements of the total logarithmic central slope of the mass profile in galaxy clusters constrain their evolution and assembly history and that of their Brightest Cluster Galaxies. We report the first full surface brightness distribution modelling of the inner region of the galaxy cluster MACS J1149.5+2223. We compare these results with a position-based modelling approach for which we employ more than twice the previously known positional constraints. This is the first time that the detailed lensed image configuration of two non-central cluster galaxies with Einstein rings has been mapped. Due to the extended radial coverage provided by the multiple images in this system, we are able to determine the slope  $\partial \log \kappa / \partial \log R = -0.37$  of the total projected mass distribution from 8 to 80 kpc. This is within the cluster-to-cluster scatter estimates from previous cluster measurements. Our reconstruction of the image surface brightness distribution of the large central spiral galaxy has a root mean square residual for all image pixels of  $1.14 \sigma$ , where  $\sigma$  is the observational background noise. This corresponds to a reconstruction of the positions of bright clumps in the central galaxy with a rms of 0.063 arcseconds.

**Key words:** Gravitational lensing – methods: observational – dark matter – galaxies: clusters: individual (MACS J1149.5+2223)

## 1 INTRODUCTION

Our current understanding of structure formation is based on a hierarchical picture where more massive Dark Matter (DM) structures form via infall and the progressive merging of smaller objects. Dark Matter only simulations of the Cold Dark Matter (CDM) paradigm over the last two decades have predicted remarkably self-similar DM mass profiles that are well fit by gradually steepening analytic models such as the Einasto (Einasto 1965) or Navarro Frenk and White (NFW) Navarro et al. (1997) profile, over a wide range of scales from galaxy clusters (Reed et al. 2005; Diemand et al. 2004; Springel et al. 2001, 2005; Merritt et al. 2006; Gao et al. 2012) to galaxies (Navarro et al. 2010). Although this general picture, a central slope  $\gamma_1 = \partial \log \rho / \partial \log r \approx -1$  and a steeper outer slope  $\gamma_2 \approx -3$  is generally accepted, the details are still being refined. On cluster scales Gao et al. (2012) found considerable ( $\sim 20$  percent) halo-to-halo scatter in a suite of nine high-resolution simulated N-body DM-only clusters. At galaxy scale, environmental and baryonic effects become increasingly important in shaping the DM mass distribution.

Gravitational lensing provides a powerful tool to compare the predictions of cluster simulations with observations. There has been considerable effort to get a coherent picture of the total clus-

ter mass distribution on a large range of scales by combining stellar kinematics at the innermost radii ( $r < 10$  kpc) with weak lensing measurements for radii  $r > 100$  kpc and strong lensing on intermediate scales (Sand et al. 2004, 2008; Newman et al. 2013). Clusters are very nonlinear systems where objects of different scale interact. For the study of cluster substructure such as cluster galaxies or DM subhalos detailed high resolution modelling is needed on an cluster-by-cluster basis.

There is no definitive prediction from numerical simulations for the asymptotic central slope of the galaxy cluster mass distribution. On scales of a few kpc the baryonic component of the BCG and the dark matter halo play comparable roles in shaping the total density. However, there are competing hypotheses about their relative importance and the relevant physical processes involved. The inner DM profiles can be steepened by adiabatic contraction (Gnedin et al. 2004; Sellwood & McGaugh 2005; Sommer-Larsen & Limousin 2010), or flattened by (repeated) ejection of gas by Active Galactic Nuclei (AGN) (Martizzi et al. 2013) or by heating by dynamical friction (El-Zant et al. 2001, 2004). Even in simulations with dissipationless mergers of multi component systems (DM+stars) a flattening of the inner DM profile can be achieved (Laporte et al. 2012).

Sand et al. (2008) combined stellar velocity dispersion observations with strong lensing data for the cluster Abell 383 and found that the inner slope of the dark matter is  $\gamma_{\text{DM}} \approx -0.45$ . This is

\* Email: rau@mpa-garching.mpg.de

shallower than the values found at similar radii in purely DM simulations. More recent observational constraints come from Newman et al. (2013). They performed a combined stellar kinematic, strong lensing and weak lensing mass reconstruction for seven massive ( $0.4 < M_{200}/(10^{15}M_{\odot}) < 2$ )<sup>1</sup> clusters with redshifts between 0.2 and 0.3. They find a 3D central logarithmic total mass density slope consistent with NFW ( $\gamma \approx -1.16$ ) with a scatter between clusters of  $\sigma_{\gamma} = 0.13$  (68%CL). This, however is the total density profile, and the central  $< 10$  kpc are typically dominated by the stars of the BCG. An analysis of the separate contributions of baryons and DM in Newman et al. (2013) indicates a flattening of the DM profile with a logarithmic central slope of  $\gamma_{\text{DM}} \approx -0.5$ .

In this paper we focus on building a high resolution lens model for MACS J1149.5+2223, comparing the slope inferred from the lensing reconstruction with the predictions for the total central mass density slope of galaxy clusters from cosmological structure formation simulations.

There are two previously published lens models for the cluster MACS J1149.5+2223. The first is by Zitrin & Broadhurst (2009). They assumed that mass approximately follows light and smoothed a superposition of power law mass profiles for each galaxy to obtain their mass model. As constraints they used multiple image positions from strong lensing, but many of the details especially for system 1 (see Sec. 2) are only reproduced approximately. They found a near-uniform DM surface mass density out to  $\sim 200$  kpc under the assumption that the BCG consists only of stellar mass.

The second model by Smith et al. (2009) is also based on the image positions of multiply lensed bright clumps. However, they identified a larger number of bright clumps in the main source which significantly increased the number of constraints. The image positions in their best model have a root mean square (rms) deviation from the observed positions of 0.5 arcsec. Their preferred mass model includes a central component and three smaller group/galaxy scale halos. However, the mass distributions of *all* (including the central galaxies except the Brightest Cluster Galaxy) are tied to their light distributions. They rule out the flat central profile proposed by Zitrin & Broadhurst (2009).

In this work, we improve on these previous models in three areas. First, we use a more sophisticated model. We model *all five* galaxies that are close to multiply lensed images and close to the cluster centre using individual mass profiles. This is crucial for reproducing the morphology of the lensed image of the main system (see Sec. 2). Second, we identify twice as many constraints as previously used. These include substructure in the Einstein rings that form around two cluster galaxies as well as details of the nonlinear configuration of the image covering the centre of the cluster. This puts tight constraints on the slope of the total mass density. Third, we use a more sophisticated method that was originally developed and applied on galaxy scales by (Koopmans 2005; Suyu et al. 2006; Vegetti & Koopmans 2009) and recently also on cluster scales by Eichner et al. (2013). In this method, we use not only information on the positions of the multiply lensed images, but also the full surface brightness distribution of the images.

This paper is organised as follows. We describe the observations, the image morphology of the main lensed image and the newly identified positional constraints in section 2. In section 3 we describe our analytic mass parametrization and in section 4 our two modelling methods. Section 5 contains the main results, the

best lens models for the position modelling and the surface brightness modelling in sections 5.1 and 5.2 respectively. The slope measurement of the total mass distribution is presented in section 6. Throughout this paper, we assume  $H_0 = 67.3$  and  $\Omega_m = 0.315$  from Planck (Planck Collaboration et al. 2013). At the redshift of the cluster,  $z = 0.544$ , one arcsec corresponds to 6.6 kpc.

## 2 OBSERVATIONS AND CONSTRAINTS

The galaxy cluster MACS J1149.5+2223 at redshift  $z = 0.54$  was observed as part of the CLASH program with the Advanced Camera for Surveys (ACS) on board the Hubble Space Telescope (HST). For details on the observations, the available filters and the imaging pipeline, we refer the reader to Postman et al. (2012). The CLASH image pipeline provides redshifts of all galaxies close to the cluster. Spectroscopic redshifts are available for the sources 1, 2 and 3 from Smith et al. (2009).

Since our lens modelling technique makes use of both the positions of the lensed images and their surface brightness distribution, it is very important to minimise the light contamination from the lensing galaxies. This is particularly true for those images that lie close to bright cluster members. In this paper, we focus on the lens modelling of the F555W filter of the ACS, this being a compromise between a high signal-to-noise ratio and weak light contamination from the cluster galaxies in a single filter. We model the surface brightness distribution of the seven galaxies, the BCG and a star close to the three main lensed images using the publicly available program galfit (Peng et al. 2002). The positions of all modelled components are summarised in Table 1. All light distributions are modelled as a Sersic profile. This step is only needed during the modelling of the full surface brightness information of the lensed images in Sec. 4.2.

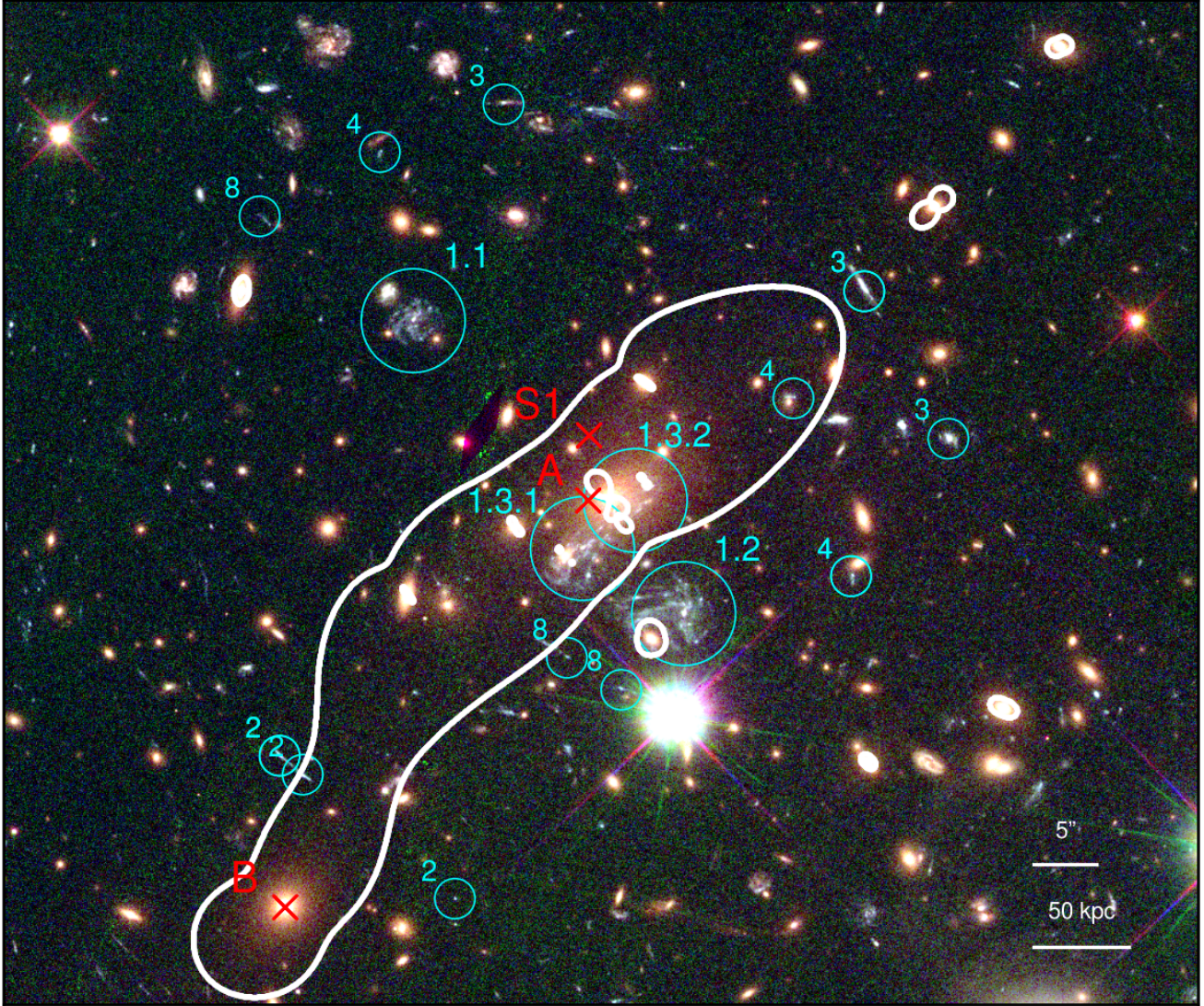
For the modelling based on the image positions only (see Sec. 4.1), the robust and correct identification of many corresponding multiply lensed source clumps is crucial. Note, that the surface brightness reconstruction in Sec. 4.2 does *not* depend on somewhat arbitrarily chosen points on the image plane since it uses the full image brightness distribution of the lensed images. We identify five different sources lensed by the cluster MACS J1149.5+2223 in as many as 15 images, here we count the main image system with a multiplicity of three according to the brightest source clump. However, some bright clumps in source 1 are lensed up to seven times. Figure 1 shows an overview of these sets of images. We follow the nomenclature of Smith et al. (2009) and Zitrin & Broadhurst (2009) to label the multiple images. Spectroscopic observations on the Keck telescope in 2004 by Smith et al. (2009) found a redshift of  $z = 1.4906 \pm 0.0002$  for the source of image system 1, sources 2 and 3 are at redshifts 1.894 and 2.497 respectively. For sources 4 and 8 we take the photometric redshifts provided by the CLASH 16 band image pipeline of 3.0 and 2.9.

Image system 1 consists of at least triple lensed images of a spatially resolved spiral background galaxy and it is currently one of the largest known gravitationally lensed image systems. For a detailed view of each of the three main images 1.1, 1.2 and 1.3 without the critical curves overlaid we refer to Fig. 2. In blue we show the constraints identified by Smith et al. (2009), in red the multiply imaged source knots that we additionally identify and use in this work.

The farthest of the three main images is 1.1, located at  $(-16.2'', 14'')$  thus about 20 arcsec from the BCG. There are no massive cluster member galaxies nearby and the two smaller close-

<sup>1</sup>  $M_{200}$  is the mass within a sphere with radius  $r_{200}$  and a mean enclosed density 200 times the critical value





**Figure 1.** HST F814W/F606W/F555W RGB colour image of the Cluster Lensing And Supernova survey with Hubble (CLASH) observation of MACS J1149.5+2223. Overlaid in white is the critical curve for a source redshift of  $z_s = 1.49$  and a cluster redshift of  $z_l = 0.544$  for our best model. The centre of the reconstructed DM halo A is  $\approx 1.5$  arcsec left of the BCG. There are three separate main images labelled 1. The detailed morphology of the central image, 1.3, is more complicated, parts have a seven fold image configuration. Additional multiple images are labelled 2-8, for details see Sec. 2.

by galaxies have no measurable lensing effect on the image surface brightness distribution. This image therefore gives a good impression of the almost unlensed source morphology. For the first time, we are able to use constraints based on the lower left part of the source, consisting of the triple imaged clumps 26 and 24 (cf. Fig. 2).

A second image 1.2 is lensed at  $(5.1'', -9.1'')$ , a distance of 11 arcseconds. If we compare the surface brightness distribution of images 1.2 and 1.1 in Fig. 2 it is evident that the lower left spiral arm of the source in image 1.2 is additionally lensed. Galaxy G2 acts as an additional strong lens and deflects the two source clumps 50 and 52 to a ‘secondary Einstein ring’ with Einstein radius of about 1.3 arcsec. Due to the additional deflection of the galaxy G2, clump 52 is lensed a total of seven times. Since the fifth image in image 1.2 is lensed very close to the subtracted lens galaxy surface brightness distribution and since the corresponding multiple images

in the main images 1.1 and 1.3 are not uniquely identifiable, we use, as constraints, only four of the seven multiple images. The high additional magnification from the galaxy G2 increases the visibility of the source clump 52 in image 1.2.

The third lensed image, 1.3, is lensed at a distance of 4.5 arcsec from the BCG at  $(-2.9'', -4'')$  and has a significantly more complicated morphology. In Fig. 2 we split this central image in two. Image 1.3.1 is a full multiple image of the source galaxy. Note the cluster galaxy G1 that lies on top of the lensed image. This galaxy is responsible for additional strong lensing in image 1.3 similar to galaxy G2 in image 1.2. The newly identified clumps 15 and 21 are additional multiple images deflected by galaxy G1. Together with the positions of the new constraints 24 and 26, the mass distribution of the galaxy G1 is now tightly constrained over a large range of radii from  $r = 0.4$  arcsec (2.6 kpc) from the galaxy centre to  $r = 23.0$  arcsec (150 kpc)

**Table 1.** Positions relative to the BCG of those galaxies whose surface brightness distribution was modelled with a Sersic profile and subtracted for the full surface brightness modelling of the lensed image system 1 in Sec. 4.2.

	$x$ [arcsec]	$y$ [arcsec]
BCG	0	0
G1	-3.6	-4.6
G2	3.2	-11.1
G3	0.5	-1.6
G4	2.6	1.4
G5	-17.6	12.9
G6	-13.8	12.5
G7	-7.6	-2.3
Star	5.1	-17.2

Finally, the most important and critical image is image 1.3.2. All multiple source clumps in this image are in the high magnification region close to the cluster centre where there are three galaxies, the BCG, and the galaxies G3 and G4. Image 1.3.2 consists of multiple images of only a few source clumps and was previously not constrained well. Here, we add the multiple source clumps 192, 8 and 6 as well as the 5th image of clump 19 between images 1.3.1 and 1.3.2 to our list of constraints. In total we identified as many as 77 image positions in system 1 that we use to constrain the central regions of the cluster mass distribution.

At large scales the mass distribution of the cluster is constrained by the triple image systems 2, 3, 4 and 8. In total, these ‘outer’ constraints add up to 12 images rising from lensed sources located at redshifts spanning from  $z = 1.5$  to  $z = 3.0$ . The lower images of systems 8 and 4 provide constraints at distances between 13 and 19 arcseconds. Most constraints of systems 2, 3, 4 and 8, however, are in the range 26 – 33 arcsec from the BCG.

### 3 THE MASS MODEL

In this section we describe the analytical mass model and free parameters used for the lens modelling. The same model is used for both, the image position modelling (Sec. 4.1) and the hybrid modelling of the image positions and the surface brightness distribution (Sec. 4.3).

Following the CDM paradigm, the parametric mass model considered in this paper includes: a central dark matter halo for the cluster A, five central mass components for the BCG and the galaxies G1, G2, G3 and G4, one mass component for a massive galaxy at B =  $(-25.7'', -32.3'')$ , and one for a group of smaller galaxies at C =  $(19.2'', 48.1'')$  from the BCG. We also include one mass component for each of all the remaining identified cluster member galaxies in a scaled manner and a contribution of external shear. Since the spiral galaxy of image system 1, hereafter S1, lies at redshift  $z = 1.49$ , it has a significant lensing contribution for the modelling of the other higher redshift sources. We therefore include a final mass component at  $z = 1.49$  and employ a multiple lens plane algorithm. Figure 3 shows the geometry of the lens planes for sources 1, 3 and 8 and the schematic light paths for sources 1 and 3 as an example. We use a nested loop and reconstruct in a first step the source for image system 1 which is not affected by S1. For the sources at higher redshifts, 2, 3, 4 and 8, we then additionally include a mass component centred at the reconstructed source S1 on a second lens plane at redshift  $z = 1.49$ .

We assume that all the mass components described above have a total mass density distribution that follows a dual softened Power-

law Elliptical Mass Distribution (dSPEMD) (Barkana 1998; Kassiola & Kovner 1993), with projected surface mass density in units of the critical density  $\kappa = \Sigma/\Sigma_c$  given by

$$\kappa(R) = n [(R^2 + c^2)^{-\gamma} - (R^2 + t^2)^{-\gamma}]. \quad (1)$$

This corresponds to a 3D density

$$\rho(r) = \tilde{n} [(r^2 + c^2)^{-\gamma_{3D}/2} - (r^2 + t^2)^{-\gamma_{3D}/2}] \quad (2)$$

$$\text{where } \tilde{n} = n \frac{\Sigma_c \Gamma[\gamma_{3D}/2]}{\sqrt{\pi} \Gamma[(\gamma_{3D} - 1)/2]}.$$

Here, the 2D slope  $\gamma$  is related to the 3D slope via  $\gamma = (\gamma_{3D} - 1)/2$ .  $R^2 = x^2 + y^2/q^2$  denotes the projected, elliptical radius, where  $q$  is the ellipticity,  $c$  the core radius and  $t$  the truncation radius. The dSPEMD profile has a total of seven free parameters  $(x, y, n, c, t, \gamma, q)$ . However, including seven parameters for each of our nine dSPEMD mass components would require an optimisation in a 63-dimensional very nonlinear parameter space, which is unfeasible. We therefore have to fix some of the parameters. In the following we summarise those choices.

We did tests during which we allowed the parameters to vary in order to identify those parameters that are not constrained by the data or that do not influence the quality of the model and that could be therefore kept fixed during the final modelling. Tests with variable slope of the cluster halo A and the BCG do not improve the modelling and converge to a value close to  $\gamma = 0.5$  (isothermal), therefore we keep the slope fixed for the final modelling and do not truncate the main halo A. We fix the ellipticity and position angle to the light distribution for the BCG and galaxies G1 and G2. For those galaxies, we assume a density distribution with vanishing core radius centred at the light distribution, while we leave the normalisation, and the truncation radius as free parameters. Tests also indicate that there is no measurable offset of the centroid of the galaxies in the cluster from the centre of their light distribution. For Galaxies G1 and G2 we additionally leave the slope of the dSPEMD as a free parameter. This is different from previous analysis of galaxy truncations, where the slope is generally kept fixed at isothermal (Suyu & Halkola 2010; Donnarumma et al. 2011; Eichner et al. 2013). This simplifying assumption is often necessary to avoid degeneracies between the slope, the normalisation and the truncation radius. In most cases of *isolated* galaxy-scale lensing there are not enough constraints on different radii to break those degeneracies since there is only information at the scale of the Einstein radius. The unique case of MACS J1149.5+2223 provides enough constraints over a large range of radii to measure both the slope and the truncation radius for both the galaxies G1 and G2. We refer the reader to the forthcoming paper Rau et al. (2014) (hereafter RVW2) for a detailed comparison of different mass models for G1 and G2. In this paper, we restrict ourselves to the best parametrization inferred in RVW2. For the galaxies G3 and G4 we also fix the position to the centre of the light distribution, the slope to isothermal and the truncation radius to 1 arcsec and 7 arcsec respectively. The galaxies B and S1 have a free normalisation parameter. The galaxy group C is modelled as a cored elliptic mass distribution where the normalisation, the core radius, the angle and the truncation radius are free to vary.

At larger radii we include *all galaxies with*  $I_{814} < 20.5$  as isothermal dSPEMD with position, ellipticity, and rotation angle fixed to the best fit parameters of their light distribution while the mass normalisation, the core radius and the truncation radius are scaled with the galaxy luminosity via the following scaling rela-



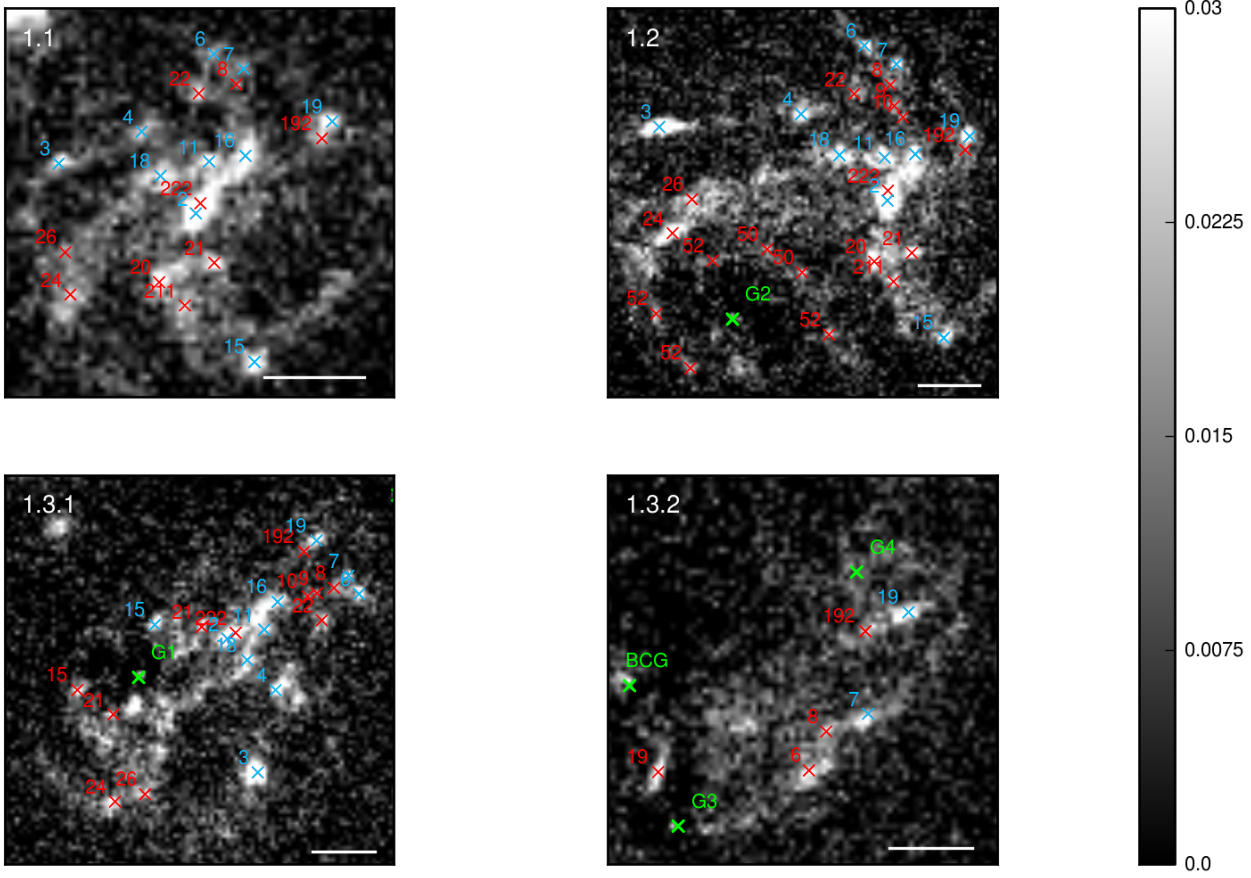


**Figure 2.** Constraints used for the image position modelling. Top left: Relatively undistorted source image. Top right: Second image with a distinct signature of an additional Einstein ring, around the satellite galaxy G2 (galaxy surface brightness subtracted). Bottom row: Strongly distorted image system 3 close to the central galaxies. Green crosses indicate galaxies G1, G2, G3, G4 and the BCG, whose surface brightness distribution we subtracted in preparation for the surface brightness modelling. Blue constraints are from Smith et al. (2009), red constraints are newly identified in this work. White line at the bottom indicates 1 arcsec scale.

tions

$$\begin{aligned} \sigma &= \sigma^* \left( \frac{L}{L^*} \right)^{1/4} \\ r_{\text{core}} &= r_{\text{core}}^* \left( \frac{L}{L^*} \right)^{1/2} \\ r_{\text{cut}} &= r_{\text{cut}}^* \left( \frac{L}{L^*} \right)^{1/2}, \end{aligned} \quad (3)$$

as previously done by Smith et al. (2009), Jullo et al. (2007) and Eichner et al. (2013). We adopt the best-fit parameters for a  $L^*$  galaxy from Smith et al. (2009),  $\sigma = 180 \text{ km/s}$ ,  $r_{\text{core}} = 0.2 \text{ kpc}$  and  $r_{\text{cut}} = 30 \text{ kpc}$ .

In previous analysis of this cluster by Zitrin & Broadhurst (2009) and Smith et al. (2009) the masses of *all* galaxies, apart from the BCG, were tied to one fiducial galaxy via Eqs. 3, while their position, ellipticity and position angle were fixed to those of their respective surface brightness distributions. In this work, instead, all five central galaxies and the three outer mass components are independently modelled. This represents a major improvement in the model, since the details of the lensing reconstruction crucially depend on the central mass distribution.

Finally, the external shear is described by a shear strength  $\gamma_s$  and a position angle  $\theta_\gamma$ , both free parameters of the mass model.

## 4 MODELLING METHODS

We model the mass distribution of MACS J1149.5+2223 with two different methods. In particular, we first build a model using the lensed image positions and the constraints introduced in Sec. 2 as described in the next section, we then refine this model with full image surface brightness distribution modelling of image 1.

### 4.1 Modelling of the Image Positions

For the image position modelling we optimise the posterior

$$P(\boldsymbol{\eta}|\mathbf{d}) \propto P(\mathbf{d}|\boldsymbol{\eta})P(\boldsymbol{\eta}) \quad (4)$$

where  $\boldsymbol{\eta}$  is a vector containing the model parameters which depends on the parametrization of the mass distribution in Eq. 1,

$$\boldsymbol{\eta} = (x_i, y_i, \theta_i, n_i, \gamma_i, c_i, \epsilon_i, t_i) \quad i \text{ in } \{1, \dots, N\}, \quad (5)$$

and  $\mathbf{d}$  is the data vector containing all of the image position constraints. The likelihood,

$$P(\mathbf{d}|\boldsymbol{\eta}) = \frac{1}{Z} \exp \left( -\frac{1}{2} \sum_i^{N_i} \delta \mathbf{u}_i^T \boldsymbol{\mu}_i^T \mathbf{C}_i^{-1} \boldsymbol{\mu}_i \delta \mathbf{u}_i \right) \quad (6)$$

$$\text{where } \delta \mathbf{u}_i = \mathbf{u}_i^{\text{obs}} - \mathbf{u}_i^{\text{mod}}$$

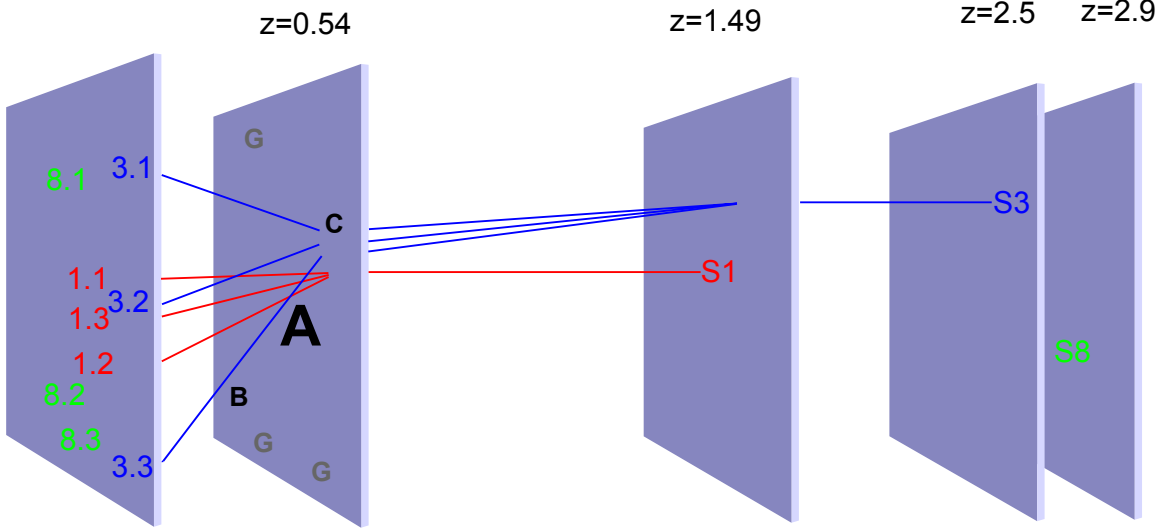


**Figure 3.** Geometry of the cluster lens and the sources S1, S3 and S8 and schematic light paths for sources S1 and S3 as an example. We include the lensing effect of the source S1 of the main image system 1, in the reconstruction of all other multiple images whose sources are at higher redshift. A,B,C denote individually modelled mass components in the cluster, G scaled galaxy mass contributions.

is defined on the source plane, which is a good and fast approximation for the true distance on the image plane (see for example Halkola et al. 2006; Suyu & Halkola 2010). Here the source plane positions are denoted  $\mathbf{u}_i$  and the sum is over the  $N_i = 3(4, 5, 7)$  images of MACS J1149.5+2223. The entries of the vectors  $\mathbf{u}_i$  for the source positions and  $\boldsymbol{\mu}_i$  for magnification contain the different constraints for each image, while the diagonal covariance matrix  $C_i$  contains the uncertainty  $\sigma_i$  of the positional data.  $Z$  is the normalisation constant  $1/(2\pi \det \mathbf{C})$ .

The speed and the power of this method depend on the number of source clumps that are identified as multiply lensed and as constraints. Compared to the modelling of the full image brightness distribution described in the next section, the position modelling only uses a very small fraction of the available information resulting in greater parameter uncertainties. However, since the evaluation of Eqs. (4) to (6) is very fast, we can use the position based modelling to rule out a big portion of the full parameter space. In practice, we include this method also in the surface brightness modelling, by disfavouring models that predict images offset from the observed true position that are separated by more than the size of the image 1.2. This is a significant speed-up for the full image brightness modelling.

#### 4.2 Modelling of the Image Surface Brightness Distribution

The full modelling of the image surface brightness information is based on the technique introduced by Suyu et al. (2006) and Vegetti & Koopmans (2009). In the following, we summarize the most important aspects of this method. At each step of the modelling, we find the best source surface brightness distribution  $\mathbf{s}$  for an observed image surface brightness distribution  $\mathbf{d}$ , source regularisation strength  $\lambda_s$  and form  $\mathbf{R}$ . For each set of lens model parameters  $\boldsymbol{\eta}$ , we find the source surface brightness distribution that maximises

the following probability density function

$$P(\mathbf{s}|\mathbf{d}, \boldsymbol{\eta}, \mathbf{R}) = \frac{P(\mathbf{d}|\mathbf{s}, \boldsymbol{\eta}, \mathbf{R}) P(\mathbf{s})}{P(\mathbf{d}|\lambda_s, \boldsymbol{\eta}, \mathbf{R})}. \quad (7)$$

The likelihood

$$P(\mathbf{d}|\mathbf{s}, \boldsymbol{\eta}, \mathbf{R}) = \frac{1}{Z} \exp \left[ -\frac{1}{2} (\mathbf{M}\mathbf{s} - \mathbf{d})^T \mathbf{C}^{-1} (\mathbf{M}\mathbf{s} - \mathbf{d}) \right]. \quad (8)$$

is a measure how well the model fits the data.  $Z$  is the normalisation,  $\mathbf{M}$  is the lensing operator relating the source plane positions to the lens plane positions via the lens equation.  $\mathbf{M}$  is calculated in each step as a lensing matrix for a set of parameters  $\boldsymbol{\eta}$ . In Eq. (8),  $\mathbf{C}$  denotes the covariance of the observed images on the image plane. For the modelling of the F555W data of MACS J1149.5+2223 we assume uncorrelated noise on the observed images with a Gaussian distribution with a RMS of  $\sigma = 0.0065$ . We choose a quadratic prior for the source,  $P(\mathbf{s}) \propto \exp(-0.5\|\mathbf{R}\mathbf{s}\|^2)$ , favouring a flat source brightness distribution. In order to accommodate the very high dynamic range of the surface brightness distribution, we use a gradient source regularisation. Since the lensed image system 1 is very large, we only consider a subset of the image plane pixels (by a factor of 5) which are lensed back to the source plane. Those points on the source plane then define the base of a Delaunay triangulation which is used to interpolate to the full data set. Implicitly finding the best source via Eq. (7) in each step, we then optimise for the best model parameters using the posterior,

$$P(\lambda_s, \boldsymbol{\eta}|\mathbf{d}, \mathbf{R}) = \frac{P(\mathbf{d}|\lambda_s, \boldsymbol{\eta}, \mathbf{R}) P(\lambda_s, \boldsymbol{\eta})}{P(\mathbf{d}|\mathbf{R})}. \quad (9)$$

#### 4.3 Hybrid modelling

When we model the surface brightness distribution of the largest image 1, we also include the positions of all other images as positional constraints. This is necessary, since none of the mass components B, C and S1 is constrained by the surface brightness information of image 1 alone. We do not include the full surface brightness

**Table 2.** Modelled mass parameters and 95% CL errors from image position modelling and from the hybrid modelling of MACS J1149.5+2223. The three blocks are main cluster parameters, galaxy parameters and the parameters of the other mass components. Parameters  $x$ ,  $y$ ,  $c$ ,  $t$  are in arcseconds, positions relative to the BCG.

Parameter	Bright. Model	Pos. Model
$x_h$	$-1.67^{+0.011}_{-0.012}$	$-1.95^{+0.28}_{-0.26}$
$y_h$	$-0.199^{+0.0109}_{-0.0096}$	$-0.53^{+0.27}_{-0.23}$
$\phi_h$	$0.605^{+0.0010}_{-0.0015}$	$0.59^{+0.031}_{-0.023}$
$n_h$	$15.76^{+0.080}_{-0.063}$	$15.0^{+0.79}_{-0.79}$
$c_h$	$11.15^{+0.032}_{-0.050}$	$12.04^{+0.91}_{-0.86}$
$e_h$	$0.4457^{+0.0025}_{-0.0015}$	$0.491^{+0.023}_{-0.023}$
$n_{BCG}$	$1.0719^{+0.0043}_{-0.0052}$	$1.015^{+0.066}_{-0.066}$
$t_{BCG}$	$20.9^{+1.2}_{-1.1}$	$23.3^{+8.0}_{-8.0}$
$n_3$	$0.3254^{+0.0022}_{-0.0020}$	$0.348^{+0.070}_{-0.062}$
$n_{g1}$	$0.2259^{+0.0081}_{-0.0063}$	$0.20^{+0.16}_{-0.12}$
$\gamma_{g1}$	$0.7558^{+0.0043}_{-0.0055}$	$0.76^{+0.15}_{-0.18}$
$t_{g1}$	$1.305^{+0.049}_{-0.064}$	$4.9^{+4.0}_{-3.5}$
$n_{g2}$	$0.3875^{+0.0035}_{-0.0027}$	$0.135^{+0.111}_{-0.080}$
$\gamma_{g2}$	$0.7274^{+0.0012}_{-0.0013}$	$0.910^{+0.081}_{-0.104}$
$t_{g2}$	$6.95^{+0.41}_{-0.46}$	$5.7^{+6.2}_{-4.7}$
$n_{g4}$	$0.2596^{+0.0027}_{-0.0021}$	$0.144^{+0.069}_{-0.084}$
$n_B$	$3.630^{+0.081}_{-0.042}$	$3.20^{+0.18}_{-0.23}$
$\phi_C$	$2.250^{+0.025}_{-0.024}$	$2.211^{+0.095}_{-0.116}$
$n_C$	$90.7^{+2.3}_{-3.5}$	$132^{+14}_{-16}$
$c_C$	$62.1^{+1.4}_{-1.6}$	$51.6^{+4.5}_{-3.0}$
$t_C$	$82.2^{+1.9}_{-2.3}$	$79.1^{+6.0}_{-4.3}$
$x_{S1}$	$-1.59$	$3.77$
$y_{S1}$	$4.92$	$13.48$
$n_{S1}$	$1.68^{+0.26}_{-0.23}$	$0.058^{+0.093}_{-0.036}$
$ \gamma $	$0.0262^{+0.0011}_{-0.0014}$	$0.0398^{+0.0075}_{-0.0085}$
$\phi_\gamma$	$2.327^{+0.012}_{-0.015}$	$1.290^{+0.134}_{-0.097}$

information of the other image systems because those images are not very extended in the observations. We therefore perform a hybrid approach where the likelihood  $P(d|\lambda_s, \eta, \mathbf{R})$  in Eq. (9) is a multiplication of the position based likelihood in Eq. (7) and the surface brightness based likelihood Eq. (8) integrated over all possible source surface brightness distributions of S1.

## 5 RESULTS

We present the results from the image position modelling first in the next section and refine this result later using the full surface brightness information of the extended lensed images in a hybrid modelling approach in Sec. 5.2. The best parameters from both modelling methods can be found in Tab. 2. Table 2 contains the centroid of this source mass component S1. This centroid position, however, is not modelled but set at the position of the reconstructed source of system 1.

### 5.1 Results from Image Position modelling

Blue squares in Fig. 4 show all the constraints that we have used in the position based modelling method as a function of their respective distance to the BCG for our best model. The y-axis is the goodness-of-fit, that is, the distance between the best modelled image position and the observed image position in arcseconds on the image plane. The rms for all constraints is 0.23 arcsec and is represented in Fig. 4 by the blue thick solid line. The constraints in image

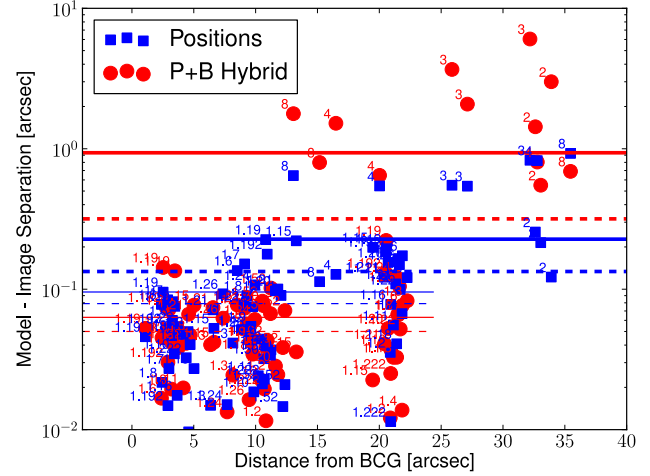


**Figure 4.** Separation of the best modelled from the true observed image position for all constraints as a function of increasing distance of the respective constraint from the BCG. Blue squares are the results from the position based modelling, red circles are the results from the surface brightness/position based hybrid modelling technique. Solid lines are the root mean square, dashed lines are the mean of the distance of the separation of the constraints. Thick lines are calculated for all constraints, thin lines the constraints in image 1 only shown in Fig. 2.

1 (cf. Fig. 2) can be found in the bulk of points in the lower half of Fig. 4. The rms of the constraints in image 1 only, 0.096 arcsec, is the blue thin solid line. The dashed lines are the mean for all and the central constraints, 0.14 arcsec and 0.08 arcsec respectively. We use a positional error in the measurements of the positions of the images in Eq. (7) of  $\sigma = 0.2$  arcsec for the central constraints in image 1 at redshift  $z=1.49$ . For the constraints in images 2, 3, 4 and 8 we use a higher uncertainty,  $\sigma = 0.78$  arcsec, since they are at higher redshifts and at least one of the multiple images of those systems is at a greater radius. This higher uncertainty leads to a radial dependence of the fit quality in Fig. 4.

### 5.2 Results from Hybrid modelling

In the last section, we did not use the majority of the observed data by concentrating on the positions of bright source clumps instead of using the full surface brightness information of the lensed images. In the following, we use a hybrid modelling approach, where we model the surface brightness of the central images plus the image positions of the outer and central images. Our hybrid modelling technique includes all the positional constraints that we used in Sec. 5.1. We will now first evaluate the results of the hybrid modelling in terms of the image positions.

The red circles in Fig. 4 show the distance between modelled and observed image positions on the image plane. The RMS distances of the separation of all (thick lines) and central (thin lines) constraints only are 0.94 arcsec and 0.063 arcsec respectively (red solid lines in Fig. 4), the means are 0.32 and 0.05 respectively (red dashed lines).

Due to the increased number of constraints, the hybrid modelling technique puts more emphasis on the accurate reconstruction of the surface brightness distribution of the central image 1. Therefore, the respective RMS is improved to a level comparable to the resolution limit of the CLASH data. Instead, the outer constraints are weighted less and consequently the image positions of the other



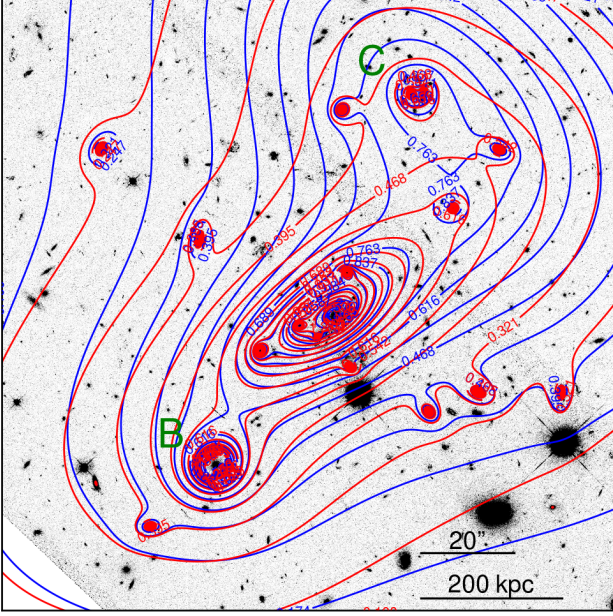


**Figure 5.** Contours of the cluster mass distribution at redshift 1.49, including scaled cluster galaxies and the two additional mass components B and C. Blue from position based modelling, red for hybrid modelling. As an orientation, the grey background shows the CLASH observation of the cluster in the F555W filter.

images are reproduced less perfectly. As a consequence, the reconstruction of all multiple images is worse in terms of the total RMS. However, the model based only on positions from Sec. 5.1 performs worse for the central image: the solution is usable as a starting point for the hybrid model, but it does not reproduce the image surface brightness distribution in detail.

Fig. 5 shows the contours of the scaled surface mass density overlaid over a grey background image of the F555W ACS observation for both our models. While the centre of the cluster mass distribution of both models is very similar, there are differences in the modelling of mass component C in the upper right. This is because this mass component is mainly constrained by the upper multiple images of systems 3 and 4 with a relatively high positional uncertainty. Those constraints therefore do not provide enough information to constrain the mass component C tightly. Figure 5 shows the integrated 2D line-of-sight  $\kappa$  contours for the main source at redshift  $z = 1.49$ . This does *not* include the mass distribution of the source S1 itself.

In the following we present the reconstruction of the surface brightness distribution of image 1 from the hybrid modelling technique. Additionally this method reconstructs the source surface brightness distribution on a nonuniform grid. Fig. 6 shows our best model of the lensed images. Each column contains one of the four main images of system 1: 1.1, 1.2, 1.3.1 and 1.3.2. In rows from top to bottom are the modelled images  $\mathbf{m}$ , the observed data  $\mathbf{d}$  and the residual  $\mathbf{r} = \mathbf{m} - \mathbf{d}$ . In the first column, image 1.1 is almost unlensed and closely resembles the original source surface brightness distribution. As a comparison, the best model of the source is shown in Fig. 7. The second image in the second column is distorted more significantly.

The aforementioned Einstein ring in image 1.2 is very accurately reproduced by our model. Note also the additional multiple images 15 and 21 (for nomenclature see Fig. 2) in image 1.3.1 and

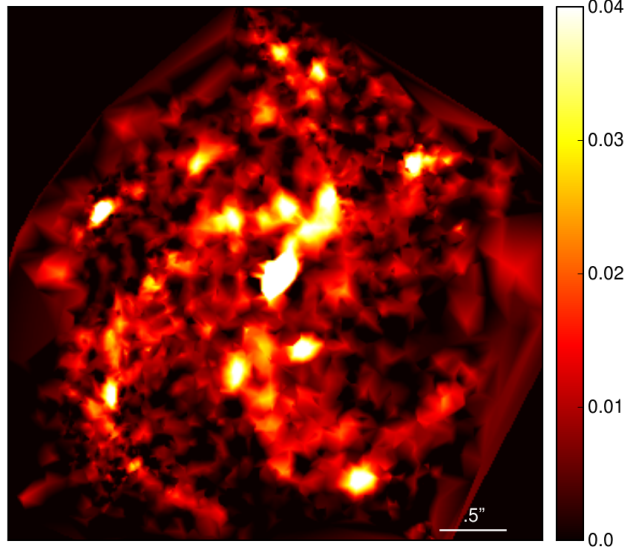


**Figure 7.** Reconstructed source brightness distribution. Colorscale is the same as in Fig. 6.

all of the morphological details of image 1.3.2 are perfectly reproduced to the noise limit of the CLASH observations. In order to quantify the residuals, we define a pixelized root mean square distance on the image plane  $\text{rms} = \sqrt{\sum_i (d_i - m_i)^2 / N}$ . Our best model has a mean square distance of  $1.14 \sigma$  averaged over the whole image 1, where  $\sigma$  is the background noise in the CLASH observations. There are minimal increased residuals at the positions of the brightest source clumps 2, 3, 15 and 19. Those are a consequence of the constant strength of the regularisation used throughout our modelling. The surface brightness distribution of the source in Fig. 7 is very nonuniform and at the edges of the brightest source clumps the gradient increases significantly, approaching infinity. This simply means that in those regions the resolution provided by CLASH is insufficient to capture the brightness distribution in detail. In this case, any form of regularisation enforces a smoothing of those regions.

It is evident from the comparison of the brightness modelling with the position modelling in Tab. 2 that the best parameters do not always agree within the error bars. This is not unexpected, since adding the surface brightness constraints to the positional constraints, we are changing the data basis for the reconstruction. Therefore, parameter regions allowed during modelling with positional constraints are discarded when the additional surface brightness information is used. Since the surface brightness contains at least two orders of magnitude more constraints and we are optimising in a 24 parameter space, the best parameters from hybrid modelling might be in a previously low probability region.

We model the mass distribution of Galaxies G1 and G2 with the profile in Eq. (1) with a variable slope. The large central images of the spiral source galaxy constrain the central 2D logarithmic slope  $\gamma' = \partial \log(\kappa) / \partial \log R$  of the two cluster member galaxies as -1.52 and -1.46 respectively (spherical deprojected -2.51 and 2.49 in 3D). The mass profile of those galaxies is therefore steeper than that of *isolated* field galaxies. For example Koopmans et al. (2006) found in the SLACS sample a 3D slope of  $\langle \gamma' \rangle = 2.01^{+0.02}_{-0.03}$  (68 % CL). Since G1 and G2 are in the dense environment of a galaxy cluster the tidal stripping of galaxy mass during the merg-



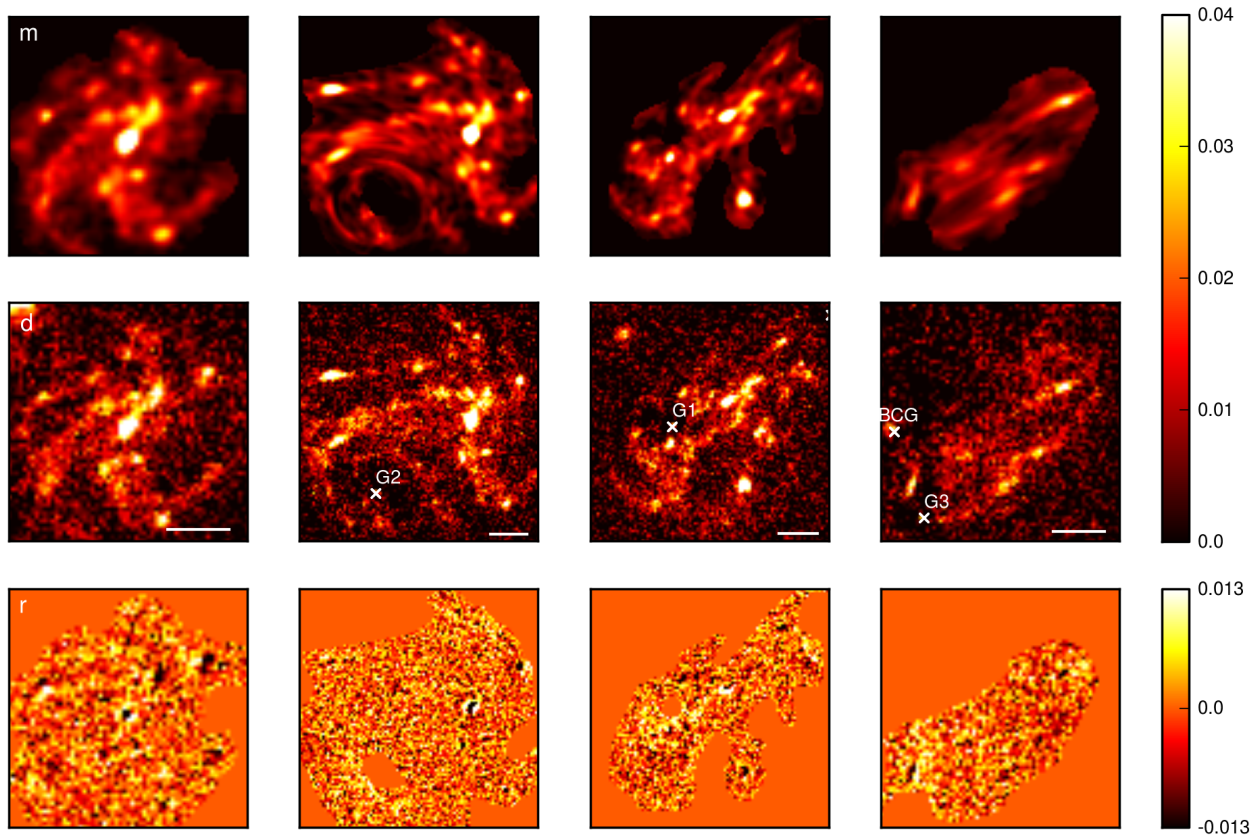


**Figure 6.** Results from the surface brightness modelling. Upper row is the model  $m$ , middle row the observed data  $d$ , lower row the residual  $r = d - m$ . Columns from left to right are the main images 1.1, 1.2, 1.3.1 and 1.3.2. Colorscale of the residual is  $2\sigma$  of the pixel noise on the image plane. Due to the high dynamic range of the source brightness distribution we use a gradient regularisation for the source brightness distribution during modelling. All features of the images are reproduced by our model down to the noise level except where the resolution of the data  $d$  is insufficient to capture the high dynamic range at the edges of the very bright source clumps. In each column, the scale of one arcsec is indicated by a white line.

ing with the cluster is a plausible hypotheses for this discrepancy (Merritt 1983, 1984, 1985; Ghigna et al. 1998; Diemand et al. 2007; Gao et al. 2012). For a detailed analysis and the comparison with different galaxy mass profiles, we refer the reader to RVW2.

### 5.3 Parameter Degeneracies

Our best model has 24 free parameters, six for the main DM halo, ten for the cluster galaxies, six for mass components farther from the BCG and two for the external shear. In order to quantify the degeneracies among these parameters, we perform an exploration of the parameter space with the publicly available library MultiNest (Feroz & Hobson 2008; Feroz et al. 2009, 2013). As an example, we show in Fig. 8 the degeneracies for a selection of nine parameters, all parameters of the central halo A and all parameters of the cluster galaxy G2. Additionally we show the normalisation, the slope and the truncation radius for the lower substructure galaxy G2. Note that we choose a flat prior between  $0.065 \text{ arcsec} < t_{G2} < 13 \text{ arcsec}$  for the truncation of the substructure galaxy G2 spanning the whole range to the central images 1.3.1 and 1.3.2 (cf. Fig. 1). In Fig. 8 we show the 68, 95 and 99.7 confidence levels (CL) from the hybrid modelling. The simpler position based modelling works well for most parameters. However, the surface brightness modelling provides a huge improvement on

the modelling accuracy and therefore has also a huge effect on the size of the confidence regions.

The most noticeable example is the truncation radius of the substructure galaxy,  $t_{G2}$  in the bottom row. Similarly to what was found by Suyu & Halkola (2010), the position modelling provides almost no constraints on the truncation radius ( $t_{G2, \text{pos}} = 5.7^{+6.2}_{-4.7} \text{ arcsec}$ ). Therefore, the surface brightness modelling is crucial in order to constrain the truncation radius. Tight constraints on all galaxy parameters such as the normalisation, the slope and the truncation radius allow us to constrain the total galaxy profile and therefore its size in detail. We find similar results for the modelling of galaxy G1. We have to keep in mind, however, that the confidence limits in Fig. 8 do *not* include systematic errors. Even though we get a very well constrained result from the surface brightness modelling, this result might be biased by the analytic form of the mass parametrization that we assume in Eq. (1). We refer to paper RVW2 for a more thorough investigation of these effects.

## 6 CENTRAL SLOPE OF THE TOTAL MASS DISTRIBUTION

Figure 9 shows the radial distribution of the projected mass density  $\langle \kappa \rangle$  for our best model, where the average is over circles centred on

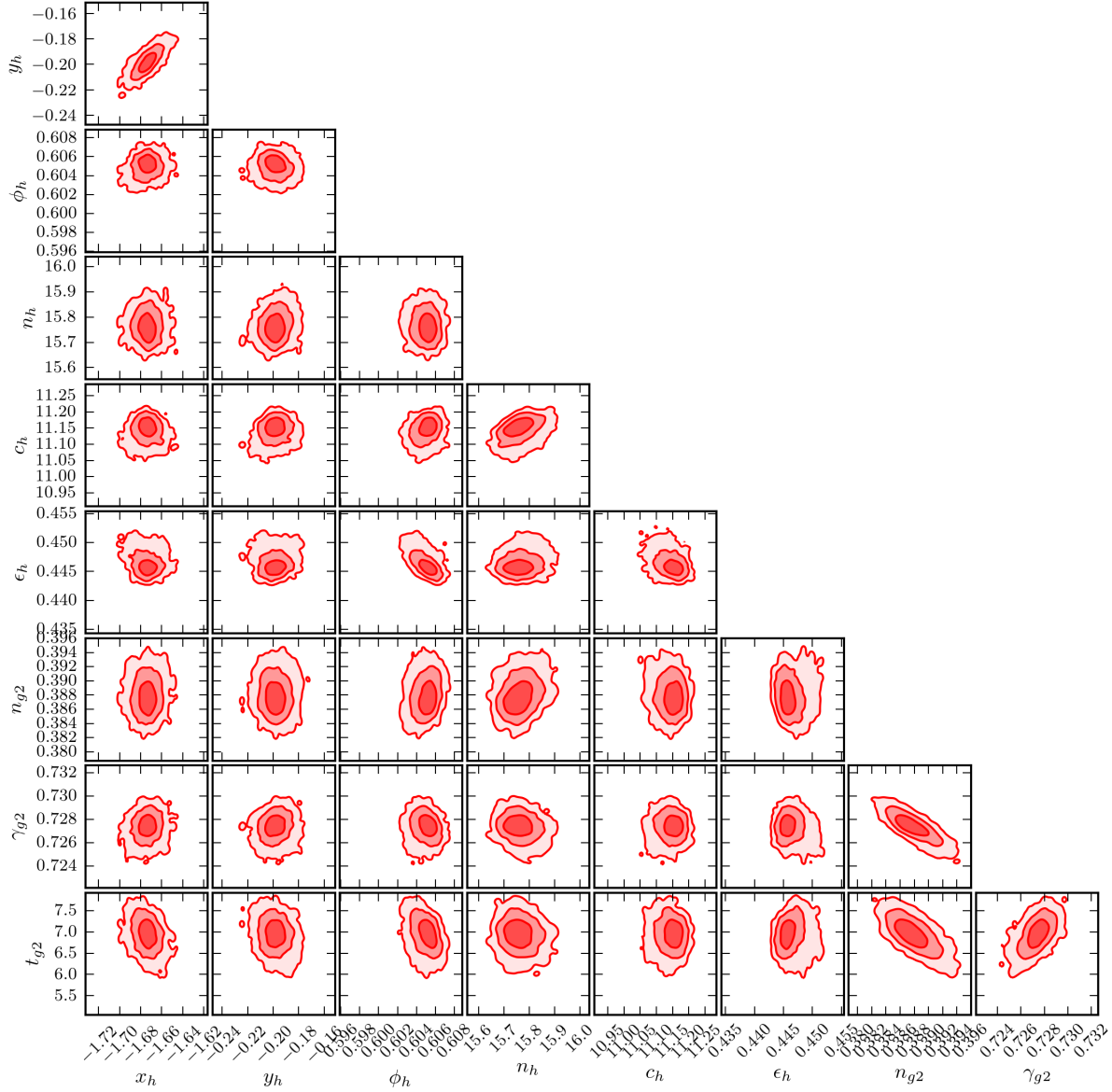


**Figure 8.** 2D marginalised posteriors for a selection of eight parameters from the full surface brightness modelling. Brightness modelling tightly constrains all model parameters, even the truncation radius of the substructure galaxy G2 in the last row, which is not constraint by position modelling only. Parameters  $x$ ,  $y$ ,  $c$ ,  $t$  are in arcsec.  $x$  and  $y$  are relative to the BCG.

the BCG. The grey shaded areas indicate the radial coverage of the main images 1.1, 1.2 and 1.3. Note, that the radial extent of the images 1.1 and 1.2 overlaps. The three main images cover almost the entire range from 0.8 arcsec to 22 arcsec (5.3 to 145 kpc). Figure 9 differentiates the contributions of the main dark matter halo, the BCG, the galaxies G1 to G4 and the mass components B and C. The dark matter component of halo A has a large core and is flat out to  $\sim 10$  arcsec ( $\sim 66$  kpc). The central cusp of the total mass distribution for  $R < 5$  arcsec (33 kpc) gets increasingly dominated by the profile of the BCG towards the centre. Due to the particular mass distribution of MACS J1149.5+2223, the contribution of the other cluster galaxies G1 to G4 to the innermost radial mass dis-

tribution is also non negligible but does not significantly affect the inferred slope (see below).

For the total mass distribution, we measure a 2D logarithmic slope of  $\gamma_{\text{tot}, 2D} = \partial \log \langle \kappa \rangle / \partial \log R$ , in the range between 1.2 and 12 arcseconds (8 to 80 kpc), this corresponds to 0.2 to  $2R_e$  for a BCG half light radius of  $\sim 6$  arcsec. This is the same range used by Newman et al. (2013). Note, that our surface brightness reconstruction of the cluster's main image system covers the whole range, so the reconstructed mass distribution is very well constrained. The straight black line in the upper panel of Fig. 9 is a linear fit in  $\log \kappa - \log R$  space (equally spaced in  $\log R$ ) to the DM halo+BCG mass density distribution. Our 2D total logarithmic

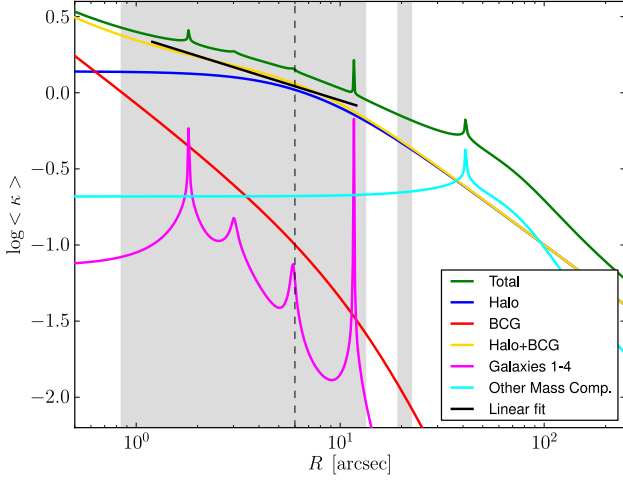


**Figure 9.** Radial distribution of the projected mass density  $\kappa(R)$  as a function of 2D radius. The constituents of the total mass profile (green) are the main DM halo (blue), the BCG total mass (red) and central cluster galaxies (magenta), outer mass components (cyan). The DM halo has a large core of  $\sim 12$  arcsec. Grey shaded areas show the radial coverage of the main image system 1. The black line is a linear fit in log-log space to DM halo+BCG mass density, for details see text. Vertical dashed line is the virial radius of the BCG.

mass density slope of  $\gamma_{\text{tot}, 2D} \approx -0.42$  is steeper than the values from the two independent measurements by Smith et al. (2009) and Zitrin & Broadhurst (2009), -0.36 and -0.24 respectively. We believe this is due to the fact that they do not include the full surface brightness distribution of the main system 1 that covers the centre of the cluster and only use  $\sim 10$  constraints in images 1.1, 1.2 and 1.3. Using spherical deprojection, our model predicts a spherically averaged 3D logarithmic slope  $\gamma_{\text{tot}} \approx -1.2$ .

Newman et al. (2013) have measured the total slope of the mass distribution (DM halo + BCG) for 7 massive clusters and have found a mean central spherically averaged logarithmic slope of  $\langle \gamma_{\text{tot}} \rangle = -1.16$  with intrinsic scatter  $\sigma_{\gamma, \text{tot}} = 0.13$  (68%CL). Our total density slope is therefore within  $0.3 \sigma_{\gamma}$  of what Newman et al. (2013) found. A certain difference is to be expected considering the differences between MACS J1149.5+2223 and the cluster sample from Newman et al. (2013): MACS J1149.5+2223 with a mass of  $M_{200} \sim 5 \times 10^{14} M_{\odot}$  is at the lower end of the mass range  $0.4 < M_{200}/(10^{15} M_{\odot}) < 2$ . The cluster is at higher redshift  $z = 0.54$  compared to their sample ( $0.2 < z < 0.3$ ) and Newman et al. (2013) choose relaxed clusters. In contrast, there are several indications that MACS J1149.5+2223 is not yet fully relaxed: a) the offset between the BCG and the cluster centre, b) the high ellipticity of the cluster mass distribution, c) close-by massive galaxies or groups of galaxies, B and D in Fig. 1 and d) non relaxed X-ray emission (see for example Fig. 3 in Smith et al. 2009).

The green line in the top panel of Fig. 9 additionally includes the mass distributions of the four central galaxies G1 to G4 and the mass components B and C. We find that in the radial range from 1.2 arcsec to 12 arcsec these galaxies contribute considerably to the total mass distribution. The total 2D density slope  $\gamma_{\text{tot}} = -0.37$  is shallower than that of the DM halo + BCG alone ( $\gamma_{\text{tot}} = -0.42$ ). In order to estimate the scatter in the slope measurement due to the galaxy subhalo population, we exclude the galaxies G1 to G4. If for example the two more distant galaxies were excluded, -G1-G2, the averaged total density slope would in-

crease to  $\gamma_{\text{tot}} = -0.40$ . Equivalently, excluding the innermost galaxies, -G3-G4, results in a decrease of the total density slope ( $-0.33$ ).

We conclude therefore that if there are cluster galaxies very close to the cluster centre, their contribution to the total potential in which the stars of the BCG form is non-negligible. It is therefore important to accurately model and to include the mass distribution of cluster member galaxies, in order to measure the total mass distribution.

Without BCG velocity dispersion measurements for MACS J1149.5+2223 it is not straightforward to separate the DM from the stellar mass content of the BCG. However, Zitrin & Broadhurst (2009) reported a mass of  $\sim 1 \times 10^{12} M_{\odot}$  for their BCG model component within the low surface brightness wings ( $\lesssim 30$  kpc), which is identical to what we find here. They claim that the mass to light radius of  $M/L_B = 4.5$  can be explained by the stellar content of a single burst stellar population formed at redshift  $z = 3$  and a mean half solar metallicity. Under this assumption, the central logarithmic slope of the dark matter content of MACS J1149.5+2223, the blue line in Fig. 9 is shallower than the NFW profile. In fact the central DM density is flat for  $r < 20$  kpc. This suggests that in the case of MACS J1149.5+2223 the baryons at the cluster centre have flattened the dark matter distribution with respect to that expected from purely dark matter simulations.

## 7 CONCLUSIONS

We have presented a new and detailed model for the centre of the galaxy cluster MACS J1149.5+2223. Our results can be summarised as follows:

- (i) In this paper we identify more than twice as many constraints based on the main system 1 as were used in previous work. Due to these new constraints, we are able to constrain three important details of the mass distribution, the individual mass distributions of two cluster galaxies G1 and G2, and, using the detailed morphology of image 1.3.2, the total mass distribution of the cluster at the innermost radii.
- (ii) We employ a multiple lens plane algorithm during reconstruction in order to properly include the lensing contribution of the mass associated with the source of the image system 1.
- (iii) We perform the first detailed brightness reconstruction of system 1. Our residuals of the surface brightness modelling are close to the noise level of the HST CLASH observations.
- (iv) The confidence regions of the full surface brightness reconstruction are significantly improved compared to the simpler position modelling.
- (v) The unique constraints of MACS J1149.5+2223 allow us to measure the mass profiles for individual cluster members. Two galaxies, G1 and G2, are modelled with a variable slope profile. We recover the central 2D logarithmic slopes  $\gamma'_{2D} = \partial \log(\kappa) / \partial \log R = -1.52$  and  $-1.45$  for G1 and G2 respectively. We refer the reader to the forthcoming paper RVW2 for a comparison of the result for different galaxy mass profiles.
- (vi) Our mass model suggests a large ( $\sim 12$  arcsec) core in the cluster DM distribution and that the total mass profile at the very centre of the cluster is dominated by the BCG. We find a central logarithmic slope of the 2D total mass distribution  $\gamma'_{\text{tot}, 2D} = \partial \log(\kappa) / \partial \log R \sim -0.42$  for the DM halo+BCG and  $\sim -0.37$  if the other central galaxies and cluster members are included.



## 8 ACKNOWLEDGEMENTS

SW is supported by Advanced Grant 246797 ‘GALFORMOD’ from the European Research Council.

## REFERENCES

- Barkana R., 1998, *ApJ*, 502, 531
- Diemand J., Kuhlen M., Madau P., 2007, *ApJ*, 667, 859
- Diemand J., Moore B., Stadel J., 2004, *MNRAS*, 353, 624
- Donnarumma A. et al., 2011, *A&A*, 528, A73
- Eichner T. et al., 2013, *ArXiv e-prints*
- Einasto J., 1965, *Trudy Astrofizicheskogo Instituta Alma-Ata*, 5, 87
- El-Zant A., Shlosman I., Hoffman Y., 2001, *ApJ*, 560, 636
- El-Zant A. A., Hoffman Y., Primack J., Combes F., Shlosman I., 2004, *ApJ*, 607, L75
- Feroz F., Hobson M. P., 2008, *MNRAS*, 384, 449
- Feroz F., Hobson M. P., Bridges M., 2009, *MNRAS*, 398, 1601
- Feroz F., Hobson M. P., Cameron E., Pettitt A. N., 2013, *ArXiv e-prints*
- Gao L., Navarro J. F., Frenk C. S., Jenkins A., Springel V., White S. D. M., 2012, *MNRAS*, 425, 2169
- Ghigna S., Moore B., Governato F., Lake G., Quinn T., Stadel J., 1998, *MNRAS*, 300, 146
- Gnedin O. Y., Kravtsov A. V., Klypin A. A., Nagai D., 2004, *ApJ*, 616, 16
- Halkola A., Seitz S., Pannella M., 2006, *MNRAS*, 372, 1425
- Jullo E., Kneib J.-P., Limousin M., Elíasdóttir Á., Marshall P. J., Verdugo T., 2007, *New Journal of Physics*, 9, 447
- Kassiola A., Kovner I., 1993, *ApJ*, 417, 450
- Koopmans L. V. E., 2005, *MNRAS*, 363, 1136
- Koopmans L. V. E., Treu T., Bolton A. S., Burles S., Moustakas L. A., 2006, *ApJ*, 649, 599
- Laporte C. F. P., White S. D. M., Naab T., Ruzsowski M., Springel V., 2012, *MNRAS*, 424, 747
- Martizzi D., Teyssier R., Moore B., 2013, *MNRAS*, 432, 1947
- Merritt D., 1983, *ApJ*, 264, 24
- Merritt D., 1984, *ApJ*, 276, 26
- Merritt D., 1985, *ApJ*, 289, 18
- Merritt D., Graham A. W., Moore B., Diemand J., Terzić B., 2006, *AJ*, 132, 2685
- Navarro J. F., Frenk C. S., White S. D. M., 1997, *ApJ*, 490, 493
- Navarro J. F. et al., 2010, *MNRAS*, 402, 21
- Newman A. B., Treu T., Ellis R. S., Sand D. J., 2013, *ApJ*, 765, 25
- Newman A. B., Treu T., Ellis R. S., Sand D. J., Nipoti C., Richard J., Jullo E., 2013, *ApJ*, 765, 24
- Peng C. Y., Ho L. C., Impey C. D., Rix H.-W., 2002, *AJ*, 124, 266
- Planck Collaboration et al., 2013, *ArXiv e-prints*
- Postman M. et al., 2012, *ApJS*, 199, 25
- Rau S., Vegetti S., Simon D. W., 2014, *in prep*
- Reed D., Governato F., Verde L., Gardner J., Quinn T., Stadel J., Merritt D., Lake G., 2005, *MNRAS*, 357, 82
- Sand D. J., Treu T., Ellis R. S., Smith G. P., Kneib J.-P., 2008, *ApJ*, 674, 711
- Sand D. J., Treu T., Smith G. P., Ellis R. S., 2004, *ApJ*, 604, 88
- Sellwood J. A., McGaugh S. S., 2005, *ApJ*, 634, 70
- Smith G. P. et al., 2009, *ApJ*, 707, L163
- Sommer-Larsen J., Limousin M., 2010, *MNRAS*, 408, 1998
- Springel V. et al., 2005, *Nature*, 435, 629
- Springel V., White S. D. M., Tormen G., Kauffmann G., 2001, *MNRAS*, 328, 726
- Suyu S. H., Halkola A., 2010, *A&A*, 524, A94
- Suyu S. H., Marshall P. J., Hobson M. P., Blandford R. D., 2006, *MNRAS*, 371, 983
- Vegetti S., Koopmans L. V. E., 2009, *MNRAS*, 392, 945
- Zitrin A., Broadhurst T., 2009, *ApJ*, 703, L132